Finite-temperature pseudospin torque effect in graphene bilayers

M. J. Gilbert*
Department of Electrical and Computer Engineering, University of Illinois, Urbana, Illinois 61801, USA
(Received 30 January 2010; revised manuscript received 14 September 2010; published 6 October 2010)

We use self-consistent quantum transport theory to investigate the influence of layer Fermi energy and temperature on the interlayer transport properties of bilayer graphene in the regime of excitonic superfluidity. We conclude that at low temperature the critical tunneling currents and quasiparticle penetration depths are well explained by the existing zero-temperature pseudospin torque model. However, when the thermal broadening associated with finite-temperature transport is included, we find that modes injected above the gap lead to increased critical interlayer currents and quasiparticle penetration in to the gapped regime beyond what current analytical models predict. We find that the increases in the critical tunneling current are due to thermal smearing smoothing out the quantum interference effects present at low temperature leading to a slower pseudospin precession about the pseudospin Bloch sphere.

DOI: 10.1103/PhysRevB.82.165408 PACS number(s): 72.80.Vp

I. INTRODUCTION

Nearly two decades of experimental[1–6] and theoretical[7–21] research has elucidated many of the exotic transport properties of semiconductor double quantum well systems at $\nu_{total}=1$. These systems possess broken symmetry states which may be classified either as an Bose-Einstein condensate (BEC) of excitons[7–12,22,23] or, equivalently, a pseudospin ferromagnet.[14–21] One constant fact is that the Kosterlitz-Thouless temperature for semiconductor double quantum-well systems at $\nu_{total}=1$ is in the millikelvin temperature regime. Graphene has given rise to additional possibilities for the observation of broken symmetry states without the presence of a magnetic field and at larger temperatures. Recent theoretical work has predicted that if one were to fabricate a bilayer heterostructure using graphene monolayers, in a fashion similar to that of the semiconducting case, then for certain interlayer separations and layer carrier concentrations, the Kosterlitz-Thouless temperature may be well above room temperature.[24–26]

Bilayers of graphene are suited to the observation of broken symmetry states at much higher temperatures as compared to that of the semiconductor bilayers due to the fact that it is atomically two-dimensional (2D) thereby significantly reducing the screening effects, and because it exhibits a band structure that is both linear and gapless which implies particle-hole symmetry. It should be noted, however, that the conclusion that broken symmetry states can exist at temperatures at and above room temperature is not without controversy. Estimates for the Kosterlitz-Thouless temperature obtained using a mean-field theory linearized version of the critical temperature (T_c) combined with static Thomas-Fermi screened interlayer interactions have been shown to produce a much lower transition temperature.[27] Nevertheless, the possibility of such a high-temperature broken symmetry state existing is not only physically interesting but could be of great technological use as a possible means of ultralow power logic operation.

While much is understood about the behavior of broken symmetry states in the double layer systems, the evolution of these states under the application of bias and at finite temperature remains one of the most studied and least understood areas. Currently, there exist two general theoretical approaches to explain the evolution of broken symmetry states under applied biases both of which are written in the pseudospin language where we view the *which layer* degree of freedom as a $S=1/2$ quantum spin. The first introduces the applied bias as a uniform magnetic field across the bilayer system.[14–16,18] This uniform magnetic field causes the pseudospins to precess about the $\hat{z}$ axis forcing an interlayer phase difference and a constantly oscillating interlayer current. Nevertheless, this theory predicts a splitting of the experimentally observed peak in the differential conductance when an in-plane magnetic field is applied to the system, which is not observed experimentally. Alternatively, to understand how broken symmetry states evolve under bias, we propose to examine the electrical transport of fermionic quasiparticles in terms of their local contact chemical potentials. As the fermionic quasiparticle are injected into the system, they will possess a pseudospin orientation which is not aligned with the system pseudospin orientation. Therefore, for the quasiparticles to move from one layer to the other the quasiparticle pseudospin orientation must precess about the $\hat{z}$ axis and will cause the overall system pseudospin orientation. This approach has been dubbed the *pseudospin torque effect*[28] after its close parallels to metal spintronics.[29,30] Because the current and pseudospin polarization distributions in a sample depend in a complex way on sample geometry and on disorder, a numerical approach, like the one describe below, is useful in assessing how interactions influence bilayer I-V curves and in determining when the bias voltage drives the system into a dynamic state. Moreover, since we are interested in bias configurations which are beyond the linear-response regime, we cannot use perturbation expansion of a tunneling Hamiltonian[12] thereby further justifying the use of a numerical method.

Perhaps more problematic is the fact that none of the theories presented earlier deal with the effects of finite temperature on the evolution of the system properties. While this is not an issue in the semiconductor case where the system temperature is extremely small, in graphene, where the broken symmetry states are predicted to exist at room tempera-

ture, the thermal effects can no longer be ignored. Here, we address interlayer transport in separately contacted nanometer length-scale graphene bilayers, with a view toward the identification of the collective transport effects and their evolution under nonequilibrium conditions at finite temperature using numerical simulations. We focus on the calculation and analysis of the critical tunneling currents,[31,32] which denote the end of coherent interlayer transport and are marked by a significant rise in the interlayer resistance for currents beyond the critical value. We apply the *pseudospin torque model* to explain the system transfer characteristics through the examination of the directionally dependent pseudospin fields, interlayer current densities, and system order parameter values obtained from the single-particle density matrix at different interlayer bias voltages.

We start in Sec. II with a discussion of the methods and the approximations that we have employed in the illustrative numerical calculations of interlayer quantum transport in the proposed regime of excitonic superfluidity which are the main subject of this paper. We perform self-consistent quantum transport calculations on graphene bilayers using Green's-function-based methods for a tight-binding model of a honeycomb lattice in the regime of exciton superfluidity. In Sec. III, we present and discuss the results of our self-consistent transport calculations. Our studies demonstrate that at zero temperatures the calculated critical currents in bilayer graphene concur with the predictions obtained by extending to graphene previous analysis of critical currents in semiconducting double quantum well systems.[12] Additionally, quasiparticle penetrations into the gapped region of the bulk at $T=0$ K which are consistent with previous predictions[24,33] when the models are extended to graphene. However, when we examine the case of finite-temperature transport ($T=150$ and 300 K) in the purported area of excitonic superfluidity, we find that the quasiparticle penetration into the bulk and critical current can no longer be adequately summarized through extension of previously presented theories. We find that the critical current can be as much as 50% larger as compared to the zero-temperature critical current and the quasiparticles can penetrate ~ 2 times deeper into the bulk of the system. We attribute these effects to the thermal smearing of the interlayer interactions and contributions of quasiparticle subbands which are excited well above the excitonic gap in the energy spectrum. The thermal smearing slows the precession of the $\hat{z}$ component about the pseudospin Bloch sphere. This is accomplished by washing out quantum interference effects seen at low temperature. Furthermore, after the critical current is exceeded, we can no longer attain a self-consistent solution between the mean-field transport equations, the interlayer interactions, and the electrostatics as expected from previous calculations.[33] The interlayer current drops very quickly from the value expected in the excitonic superfluid regime to that of the noninteracting electron-hole liquid. With this drop, we also see a disappearance of the excitonic gap in the energy spectrum at both low and room temperatures at which point quasiparticle currents begin to flow in the bulk of the system. This behavior may explain some of the previous transport experiments performed in the quantum-Hall regime.[32] Finally, in Sec. IV, we summarize our results.

II. BILAYER GRAPHENE PSEUDOSPIN TRANSPORT THEORY

Our theory begins with the tight-binding description of the single-layer Hamiltonian in which the unit cell has two atoms corresponding to the two intertwined A and B,

$$H_{layer} = \sum_{i,j} \tau_{ij}|i\rangle\langle j| + V|i\rangle\langle i|, \tag{1}$$

where in Eq. (1), $\tau_{ij}=-\tau=-3.03$ eV if the orbitals corresponding to $|i\rangle$ and $\langle j|$ are nearest neighbors, of which each atom has three, on the graphene layer honeycomb lattice and $\tau_{ij}=0$ otherwise. The resulting band structure is linear in nature a for the low-energy excitations and contains two minima at K and K' in the Brillouin zone as is expected from its SU(4) group symmetry. Due to its unique band structure, the quasiparticle excitations are equivalent to that of Dirac quasiparticles or equivalently Weyl neutrinos.[34,35] The $V|i\rangle\langle i|$ term in the layer Hamiltonian represents the Hartree term for each position in the layer. From the layer Hamiltonian, it is simple to extend this to the definition of the system Hamiltonian,

$$\mathbf{H} = \begin{bmatrix} H_{TL} & \mathbf{\Delta} \\ \mathbf{\Delta} & H_{BL} \end{bmatrix}, \tag{2}$$

where the diagonal portions of the system Hamiltonian represent the individual layer Hamiltonians for the top and bottom layers and the off-diagonal terms represent the interlayer interactions. It should be noted that in Eq. (1), we do not include the intralayer exciton-exciton dipole-dipole interactions. We describe our representation of interlayer interactions in graphene bilayers using a pseudospin language. If we take the top layer as the pseudospin up state ($|\uparrow\rangle$) and the bottom layer as the pseudospin down state ($|\downarrow\rangle$), the single-particle interlayer tunneling term contributes a pseudospin effective field $\mathbf{H}$ with magnitude $2\Delta_{sas}$ and direction $\hat{x}$, where Δ_{sas} is the single-particle interlayer tunneling amplitude. In the case of real spin it is well known that interactions contribute a Zeeman field to the quasiparticle Hamiltonian of a spin-polarized gas which is oriented in the same direction as the spin polarization. Bilayers with pseudospin polarization due to tunneling have a similar interaction contribution to the quasiparticle Hamiltonian.

The interaction contribution to the interlayer transport present in Eq. (1) can be derived by expanding the energy functional obtained by minimizing the Hartree-Fock trial wave function for the many-body system around the supercurrent state as has been done previously in the quantum-Hall regime.[8–10,20,36] Including both single-particle and interaction contributions we can write[28,33]

$$\mathbf{\Delta} = \Delta_{sas}\hat{x} + Um_{ex}[\cos(\phi_{ex}), \sin(\phi_{ex})], \tag{3}$$

where $\mathbf{m}_{ex}$ is the magnitude of the pseudospin polarization and is defined as

$$\mathbf{m}_{ex} = \frac{1}{2}\mathrm{Tr}[\rho_{ps}\tau], \tag{4}$$

ρ_{ps} is the Hermitian 2×2 pseudospin density matrix,

$$\rho_{ps} = \begin{bmatrix} \rho\uparrow\uparrow & \rho\uparrow\downarrow \\ \rho\downarrow\uparrow & \rho\downarrow\downarrow \end{bmatrix} \tag{5}$$

and $\tau = \sigma_x, \sigma_y, \sigma_z$ is the vector of Pauli spin matrices. In Eq. (3), ϕ_{ex} is the planar orientation of the pseudospin field on the pseudospin Bloch sphere. To define the planar orientation of the pseudospin field, we must examine each of the directional components of the planar pseudospin field. To obtain these planar directional pseudospin fields, we examine ρ_{ps} as

$$\langle m_{ex}^x \rangle = \rho\uparrow\downarrow - \rho\downarrow\uparrow,$$

$$\langle m_{ex}^y \rangle = i\rho\uparrow\downarrow + i\rho\downarrow\uparrow. \tag{6}$$

From these directional pseudospin fields, it is then easy to define the orientation of the pseudospin magnetization as

$$\phi_{ex} = \arctan\left(\frac{\langle m_{ex}^y \rangle}{\langle m_{ex}^x \rangle}\right). \tag{7}$$

But to this point we have neglected the $\hat{z}$-directed pseudospin field which is a measure of the screening between the two Fermi surfaces in the top and bottom layer and serves to separate them in energy. The $\hat{z}$-directed pseudospin field is defined as the difference between the self-consistent layer potentials in the top and bottom layer obtained from the full solution of the Poisson equation in three dimensions as

$$\langle m_{ex}^z \rangle = \frac{\rho\uparrow\uparrow + i\rho\downarrow\downarrow}{2} = \frac{V_\uparrow |i\rangle\langle i| - V_\downarrow |i\rangle\langle i|}{2}. \tag{8}$$

To be explicit, we can collect all of the interaction terms and rewrite Eq. (3) as

$$\mathbf{\Delta} = (\Delta_{sas} + U m_{ex}^x)\sigma_x + U m_{ex}^y \sigma_y + m_{ex}^z \sigma_z. \tag{9}$$

The on-site Coulomb term U in Eqs. (3) and (9) is discussed in more detail below.

To understand the evolution of the system under applied bias, we recognize that the transport properties in bilayer graphene depend only on the quasiparticle Hamiltonian and on the chemical potentials in the leads. Because the pseudospin effective field is the only term in the quasiparticle Hamiltonian which does not conserve the $\hat{z}$ component of the pseudospin, it follows that every quasiparticle wave function satisfies

$$\partial_t m_{ex}^z = -\nabla \cdot \mathbf{j}^z + \hbar^{-1}(\mathbf{m}_{ex} \times \mathbf{H})_z = 0, \tag{10}$$

where $\mathbf{j}^z$ is the $\hat{z}$ component of the pseudospin current contribution from that orbital, i.e., the difference between bottom and top layer number currents. For steady-state transport, the quasiparticles satisfy time-independent transport equations so that, summing over all orbitals,

$$m_{ex} H \sin(\phi_{ex} - \phi_H) = \hbar \nabla \cdot \mathbf{j}^z, \tag{11}$$

where ϕ_H is the planar orientation of $\mathbf{H}$. The pseudospin orbitals do not align with the external field because they must precess between layers as they transverse the sample. The realignment of transport orbital pseudospin orientations alters the total pseudospin and therefore the interaction contribution to $\mathbf{H}$. We refer to the change in $\mathbf{m}_{ex} \times \mathbf{H}$ due to transport currents as the pseudospin torque effect.

Another way of visualizing the effects of the directional pseudospin fields is to consider the pseudospin Bloch sphere. The poles of the pseudospin Bloch sphere represent quasiparticles localized in either the top layer or the bottom layer and these are represented by the $\langle m_{ex}^z \rangle$ part of the Hamiltonian. Tunneling that we consider here leads to a coherent evolution of the quantum state on the pseudospin Bloch sphere along its azimuthal angle and is represented by the longitudinal and transverse pseudospin fields $\langle m_{ex}^x \rangle$ and $\langle m_{ex}^y \rangle$, respectively. Therefore, if we inject a quasiparticle into the top layer with one pseudospin and collect it in the other layer, which contains the opposite pseudospin then the pseudospin must precess about the Bloch sphere in order to change its pseudospin orientation. While $\langle m_{ex}^x \rangle$ and $\langle m_{ex}^y \rangle$ represent the relative phase between the two layers, $\langle m_{ex}^z \rangle$ represents the motion of the quasiparticles between the two layers.

If Δ_{sas} is small compared to $U m_{ex}$ and the current is sufficiently large, greater than the critical current, it is clear that Eqs. (3) and (10) cannot be solved simultaneously, implying that there are no time-independent solutions of the transport equations. This is the type of phenomena which leads to periodic magnetization dynamics in ferromagnetic metals.[37] In the case of bilayers it has been suggested[38] that periodic pseudospin magnetization dynamics can be driven by a current when steady-state solutions are unavailable. One important type of behavior that occurs in metals is current driven switching between two different metastable magnetic states. This kind of bistability does not occur in bilayers so there is no behavior analogous to current-driven switching.

A. Hartree-Fock model of interlayer interactions

With the basic properties of the system Hamiltonian defined, we must now take a closer examination of the form of the interlayer interactions. We wish to formulate a model for the interlayer exchange which is accurate within the Hartree-Fock mean-field representation which are added to the system Hamiltonian,

$$H_{int} = \sum_\lambda = \langle i', \alpha' : \lambda | V | \lambda : \alpha, i \rangle n_\lambda, \tag{12}$$

where in Eq. (12) i represents the tensor product of the graphene sublattice pseudospin degree of freedom and the physical layer degree of freedom, n_λ represents the number of occupied eigenstates, and the sum is performed over all of the system eigenstates. Equation (12) can be easily reduced to

$$H_{int} = \sum_\lambda \langle i', \alpha' | V_{mf} | \alpha, i \rangle. \tag{13}$$

Equation (13) can be further simplified into a more useful form by using well-known properties of the single-particle density matrix as

$$\langle i', \alpha' | V_{mf} | \alpha, i \rangle = -\sum_{jj', \beta\beta'} \langle i', \alpha' : j, \beta' | V | \alpha, i \rangle n_\lambda \langle j' \beta' | \lambda \rangle \langle \lambda | j \beta \rangle, \tag{14}$$

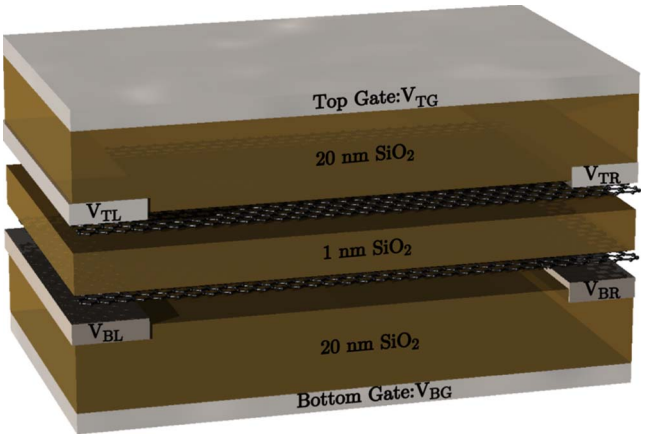

FIG. 1. (Color online) Generic schematic of the simulated device geometry. Contacts are attached to the edges of each of the layers to inject and extract current. In this work we hold the layer widths, the length of the layers, and the thicknesses of the different oxide regions fixed.

$$\langle i',\alpha'|V_{mf}|\alpha,i\rangle = -\sum_{jj',\beta\beta'} \langle i',\alpha':j,\beta'|V|\alpha,i\rangle\langle j'\beta'|\rho|j\beta\rangle \tag{15}$$

or in real space,

$$H_{int} = -U\rho(i'r{:}ir). \tag{16}$$

Equation (16), tells us that the final form of the real-space interactions between the two layers in diagonal in pseudospin layer index and its strength is characterized by the aforementioned on-site Coulomb term which, in the remainder of this paper, is taken to be 10% of the Fermi energy in accordance with earlier mean-field predictions.[24]

B. Simulation details

We conclude this section by briefly describing the methods that we use to simulate bilayer tunneling *I-V* characteristics. The calculation strategy follows a standard self-consistent field procedure. To find the single-particle density matrix of the 2D system, we must evaluate the mean-field quasiparticle Hamiltonian. For the interlayer tunneling part of the Hamiltonian we use the local-density approximation outlined above. The electrostatic potential in each layer is calculated from the charge density in each of the 2D layers by solving the Poisson equation in three dimensions with appropriate boundary conditions. The boundary conditions employed in this situation are hard-wall boundaries on the top and sides of the simulation domain and Neumann boundaries at the points where current is injected and extracted. Given the mean-field quasiparticle Hamiltonian and voltages in the leads, we can solve for the steady-state density matrix of the two-dimensional bilayer using a Green's-function-based method in a real-space tight-binding basis as done previously.[34,39,40]

The simulation geometry for our system is shown in Fig. 1. We have contacts to the edges of each of the layers to inject and extract current. We use a top and bottom gate to manipulate the quasiparticle concentrations in each of the layers. The top and bottom gates are separated from the graphene layers through by 20 nm of SiO_2. The two graphene layers are separated from one another by 1 nm SiO_2 so as to be in the regime of superfluidity predicted by many-body calculations.[24–26] We consider the oxide regions to be perfect in the sense that they do not contain any stray charges and have perfect interfaces with the graphene layers. We choose the $\hat{x}$ direction to lie along the length of the system, the $\hat{y}$ direction to lie along the width, and the $\hat{z}$ along the depth. We set the length of the layers to be 100 nm and the width of the layers to be 40 nm for all of the simulations presented. In our simulations we set contacts at the left-hand side and right-hand side of the top layer to inject current and the current is extracted through contacts on the left- and right-hand sides of the bottom layer. We assume that there is perfect registration between the graphene atoms in the top layer and graphene atoms in the bottom layer. The density matrix obtained from the quantum transport kernel is updated at each state in the iteration process using the Broyden method[41] to accelerate self-consistency. The updated density is then fed back into the Poisson solver. The effective interlayer tunneling amplitudes are also updated and the loop proceeds until a desired level of self-consistency is achieved. In this work, we define self-consistent convergence as the point in the iteration process where the difference in the old and new electrostatic potentials is less than that of the single-particle energy splitting between the two layers. The quasiparticle transport properties between contacts "A" and "B" are calculated after self-consistency is achieved via the Landauer formula at finite temperature, i.e., using

$$I(V_{AB}) = \frac{2e}{h}\int T(E)[f_A(E) - f_B(E)]dE. \tag{17}$$

III. PSEUDOSPIN TRANSPORT IN BILAYER GRAPHENE

A. Zero-temperature results

We begin our analysis of the interlayer transport properties of bilayer graphene by examining its properties at zero temperature. Before we discuss the transport properties of the system, it is important to know whether or not we have an exciton condensate established in our numerical model. A simple way of determining the properties of a condensate is through analysis of the order parameter and this is the path we follow here. We define our order parameter, written in the pseudospin language, for the exciton condensate in a bilayer system to be[33]

$$\Phi(\mathbf{r}) = |\Phi(\mathbf{r})|e^{\phi_{ex}} = \langle \hat{\psi}^\dagger(\mathbf{r})_\uparrow \hat{\psi}^\dagger(\mathbf{r})_\downarrow \rangle, \tag{18}$$

where in Eq. (18) $\hat{\psi}^\dagger$ and $\hat{\psi}$ are the electron creation and annihilation operators and ϕ_{ex} is the condensate phase defined above as the azimuthal angle of the pseudospin Bloch sphere in Eq. (7).

The order parameter should be nonzero only when coherence has been established between the top and bottom layers.

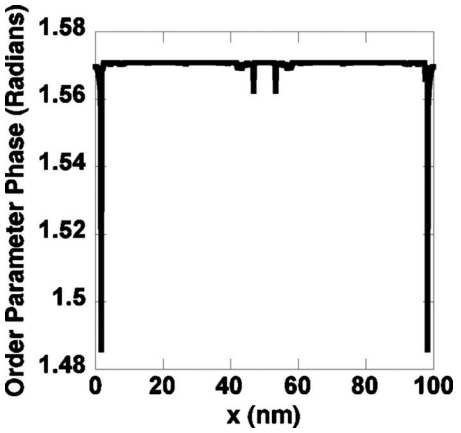

FIG. 2. Plot of the value of the order parameter plotted down the centerline of the system in equilibrium at $T=0$ K. We see that the order parameter has a nearly constant, nonzero value across the system which is indicative of the presence of a condensate.

We determine the value of the order parameter for our bilayer system first by setting the value of each contact potential to zero and performing a self-consistent calculation. The gate voltages are set to be $V_{tg}=-V_{bg}=400$ mV which corresponds to an electron and hole density of $n_e=n_h=1\times10^{13}$ cm^{-2} which places the system firmly in the dense electron-hole regime where we expect the electron-hole pairs to form a BCS-type state. This is as opposed to the dilute limit of electron-hole densities which can be described as a weakly interacting Bose system of excitons.[13] We choose a single-particle tunneling amplitude of $\Delta_{sas}=100$ μeV. The value of Δ_{sas} has been chosen to be small enough to separate the layers from one another and allow the BEC to form in our simulations but not so small as to require a significant number of loops to achieve self-consistency. In Fig. 2, we plot the condensate order parameter along the center line of the system. We choose to use a line plot rather than use the full surface plot of the order parameter as the variations about the whole of the surface differ from those shown in Fig. 2 by less than 10% and the variations are all close to the contacts. We see clear evidence of the formation of the condensate as the order parameter has taken on a nearly constant, nonzero phase across the entire system. The discrepancies from the uniform phase are attributed to some local variations in the level of self-consistency obtained across the system. The discrepancies are most prevalent near the contact points where interference effects can cause potential fluctuations.

Further insight into the nature of the excitonic superfluid formed in the graphene bilayer system by examining the directional pseudospin magnetizations at equilibrium obtained from the self-consistent density matrix. In Fig. 3, we plot $\langle m_{ex}^y\rangle$ and $\langle m_{ex}^x\rangle$ corresponding to the order parameter shown in Fig. 2. It is clear that while the order parameter stays pinned at $\frac{\pi}{2}$ across the system, the pseudospin magnetizations vary in quite a complex fashion. $\langle m_{ex}^y\rangle$ is roughly two orders of magnitude larger than $\langle m_{ex}^x\rangle$. As we are at $T=0$ K, we are injecting states directly into the gapped region. Therefore, as we inject the states into the gap, we expect to see reflections similar to those of Andreev reflections in a superconductor. The difference is that now when we inject an electron in the top layer it reflects off of the gapped region and is transmitted in the bottom layer as an electron with opposite momentum. To conserve current, the system then launches an exciton which propagates across the gapped bulk until it reflects again off of the contacts on the other side of the system, as supercurrents are not allowed to enter the contacts. This situation is visualized in the plots of $\langle m_{ex}^y\rangle$ and $\langle m_{ex}^x\rangle$. We see in both plots that the quasiparticle wave functions are only allowed to penetrate into the gapped region over a short distance corresponding to the coherence length, similar to that of a Josephson length in a BCS superconductor, of the system which we define as

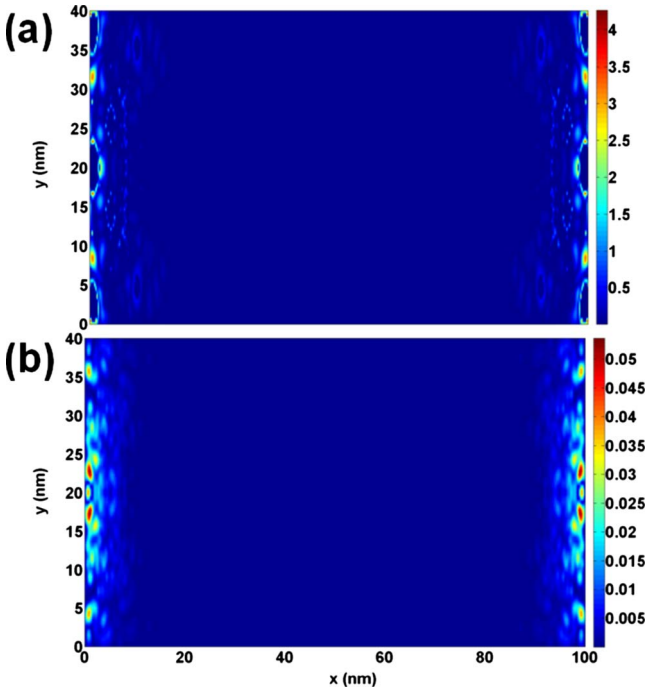

FIG. 3. (Color online) Surface plots of the directional pseudospin fields (a) $\langle m_{ex}^x\rangle$ and (b) $\langle m_{ex}^y\rangle$ computed from the self-consistent density matrix for $V_{tg}=-V_{bg}=0.4$ V.

$$L_c=\frac{1}{k_f}\sqrt{\frac{\langle m_{ex}^x\rangle}{\Delta_{sas}}}, \tag{19}$$

where in Eq. (19), E_g is the total gate voltage applied between the two layers and v_f is the Fermi velocity in graphene which here is taken to be 10^8 m/s. The resultant coherence length for this particular gate voltage configuration is $L_c=10.47$ nm and can be seen in Fig. 3 in both $\langle m_{ex}^y\rangle$ and $\langle m_{ex}^x\rangle$. Moreover, we find that while the quasiparticle wave functions decay rapidly they are still nonzero at all points, even deep within the condensate, which leads to the large current flows between the two layers.

With confidence that we have an exciton condensate formed in the system, we now wish to examine the dynamics of these states. Before descending to our numerical simulations, we can make some simple estimates as to what we expect. We do so by extending the analysis of double-layer quantum-Hall systems at $\nu=1$ to suit our graphene model.

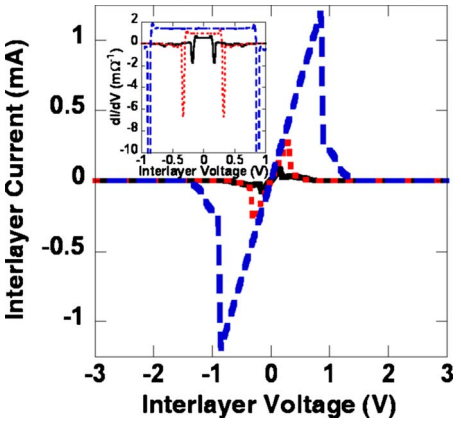

FIG. 4. (Color online) Plot of the interlayer current versus the applied interlayer voltage for gate voltages of $V_{tg}=-V_{bg}=200$ mV (solid black), 400 mV (dotted red), and 600 mV (dashed blue). The inset shows the differential interlayer conductance as a function of the applied interlayer voltage for $V_{tg}=-V_{bg}=200$ mV (solid black), 400 mV (dotted red), and 600 mV (dashed blue). This gives a much clearer picture of the location of the critical currents in our simulations.

Recalling that the ground state of these systems is described by the well-known many-body wave function,[8,9,42]

$$|\Psi\rangle = \prod_m (c^\dagger_{m\uparrow} + e^{i\phi_{ex}} c^\dagger_{m\downarrow})|0\rangle. \tag{20}$$

The exciton condensate present in the system may carry a current by adjusting ϕ_{il}. It can be shown that the maximum current that the can be carried coherently in the system is

$$I_{crit} = \frac{e\langle m^x_{ex}\rangle}{\hbar L_c^2} \times \text{Area}. \tag{21}$$

In order to support the steady-state exciton supercurrent, we follow the prescription laid out previously and bias the leads of our system in the drag counterflow geometry, in which the bias voltage is contained entirely within the top layer with $V_{interlayer}$ on the top left contact (V_{TL}) and $-V_{interlayer}$ on the right contact (V_{TR}), for the remainder of the calculations presented in this work.

In Fig. 4, we use the aforementioned bias configuration and plot the resultant interlayer current versus the applied interlayer voltage for gate voltages (Fermi energies) of $V_{tg}=-V_{bg}=200$ mV, 400 mV, and 600 mV corresponding to electron and hole densities of $n_e=n_h=5\times10^{12}$ cm^{-2}, 1×10^{13} cm^{-2}, and 1.5×10^{13} cm^{-2}, respectively. We are plotting the current that is flowing from the top left contact (V_{TL}) into the bottom left contact (V_{BL}) though it is identical to that flowing from the bottom right contact (V_{BR}) to top right contact (V_{TR}). There is no quasiparticle component of the current flowing horizontally across either the top or bottom layer. This is due to the fact that when we have an exciton condensate formed, it produces a gap in the system at the Fermi energy. In Fig. 4, we see two very distinct regions corresponding to vastly different transport regimes. For small applied interlayer biases, we see that the interlayer current increases linearly with the applied interlayer voltage corresponding to the region characterized by the coherent interlayer transport. However, past the critical interlayer current the interlayer conductivity drops very rapidly as the system has now entered high resistivity regime where the majority of the interlayer current is carried by incoherent tunneling whose value is limited by the strength of Δ_{sas}.

In order to be more specific about the location of the critical currents in Fig. 4, we look at the inset where we plot the differential conductance as a function of the interlayer bias. Here it becomes obvious that the critical currents for each different gate voltage combination occur at interlayer voltages of $|V_{crit}|=150$ mV, $|V_{crit}|=300$ mV, and $|V_{crit}|=850$ mV which correspond to interlayer currents of $|I_{crit}|=81.4\pm6.1$ μA, 279.8 ± 25.6 μA, and 1.20 ± 0.03 mA for gate voltage combinations of $V_{tg}=-V_{bg}=200$, 400, and 600 mV which are in good agreement with the predicted values for the critical currents of $|I^{anal}_{crit}|=86.8$, 355.3 μA, and 1.20 mA for a system with a stated value of $\Delta_{sas}=100$ μeV as computed using Eq. (21). The value of Δ_{sas} has been chosen to be small enough to separate the layers from one another and allow for the BEC to form but not so small as to require a significant number of loops to achieve self-consistency. We have additional evidence beyond the end of the constant differential conductance to signal the current surpassing the critical currents in that the self-consistent solutions to the mean-field transport equations can no longer be obtained. It is for this reason that we cannot make any physically meaningful statements about the subtle rise in the differential conductance just beyond the critical current observed in our simulations. These rises are not seen experimentally in the quantum-Hall samples[31,32,43] and we categorize them as a numerical artifacts. However, we should be careful to note that the lack of a time-independent, self-consistent, mean-field solution does not indicate that there is no solution to the problem. Rather, we interpret it as the onset of a metastable state in which the pseudospin orientation oscillates. Such oscillations have also been predicted to occur in metallic ferromagnets[29,37] and which may, in principle, be observed using a time-dependent method.

While it is important to understand the composition and magnitude of the current, where the current is flowing in the system is also vital to understanding this system. Given the complicated nature of the of the pseudospin magnetizations shown in Fig. 3 for a system that has no disorder in the graphene lattice or stray charges in the oxides, one would assume that there would be a similarly complicated spatial dependence of the interlayer current. In Fig. 5 we plot the interlayer currents for interlayer biases of (a) $V_{interlayer}=1$ mV and (b) $V_{interlayer}=1500$ mV corresponding to $V_{tg}=-V_{bg}=400$ mV. In Fig. 5(a), we are well below the critical current and all of the transport between the two layers is coherent. As before, electrons are injected into the gapped region and are either transmitted to the bottom layer by way of reflection off of the gap or reflected back to the injecting contact. This action gives rise to a significant amount of quantum interference from the states reflected off of the gap at the Fermi energy and the injected modes. As the injected modes may not propagate from the side of one layer and exit on the other side of the same layer, the modes have only a choice of being reflected or transmitted to the other layer. We

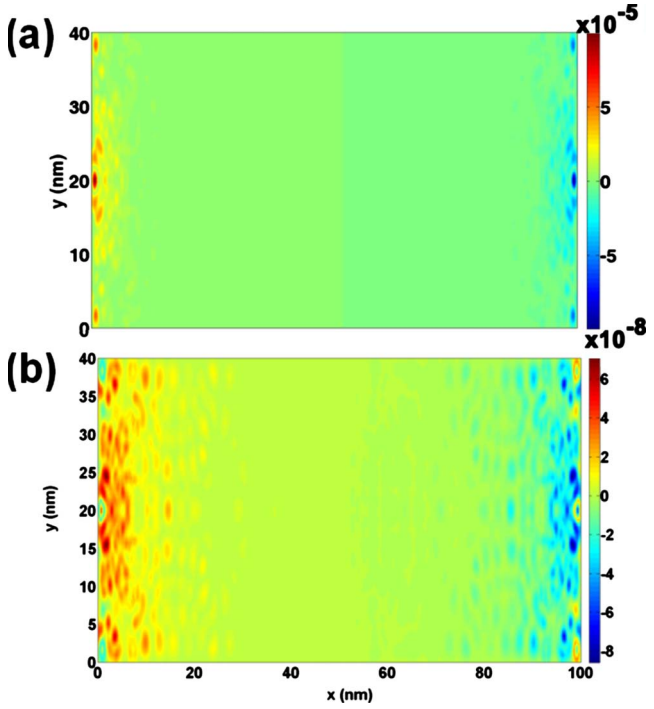

FIG. 5. (Color online) Surface plots of the interlayer current for interlayer voltages of (a) $V_{interlayer}=1$ mV and (b) $V_{interlayer}=1500$ mV the scales of both plots are in amperes. Note that the current flow between the two layers before the critical current is within L_c of the contacts but past the critical current we see charge transfer over a much greater region.

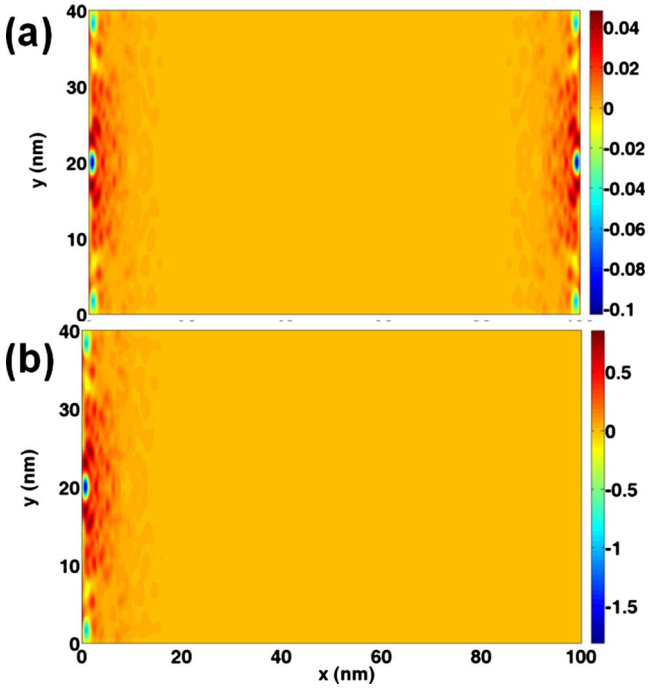

FIG. 6. (Color online) Surface plots of the directional pseudospin fields (a) $\langle m_{ex}^x \rangle$ and (b) $\langle m_{ex}^y \rangle$ computed from the self-consistent density matrix with $V_{tg}=-V_{bg}=400$ mV for interlayer voltage of $V_{interlayer}=1$ mV. As we are still in the regime dominated by exciton condensation, the pseudospin fields are appreciable only within L_c of the contacts. The scale on both plots is electron volt.

notice in that the interlayer current is bunched near the center of the system close to both contacts. On the right-hand side, we have quasiparticles moving from the bottom layer to the top layer with an identical current flow from the top to the bottom on the left-hand side. We also observe that the quasiparticle current only flows between the two layers over a distance of L_c on both sides of the system. This picture is contrasted by Fig. 5(b) where we plot the interlayer current at an interlayer voltage of 1500 mV which produces a current which is well beyond the critical current. Here we see that the interlayer current is still bunched near the center of the system but now current is no longer constrained to flow within a distance of L_c of the contacts and flows between the layers throughout the system. Moreover, we see that the current flowing from the top to the bottom on the left side is no longer equal to the current flowing from the bottom to the top on the right side. These two observations indicate that the condensate gap has closed and tunneling is now dominated by incoherent single-particle physics. The closing of the excitonic gap and emergence of a induced coherence regime could explain the nearly conserved layer currents in the bilayer quantum-Hall counterflow experiments[1,3] and which has been recently experimentally confirmed.[44]

To be more concrete about the nature of the system prior to and beyond the critical current, we examine the directional pseudospin magnetizations for at two different interlayer voltages. First, in Fig. 6 we examine the pseudospin fields for an interlayer voltage of 1 mV which is well within the regime of exciton condensation. As is the case earlier when we examined the pseudospin fields for the system in equilibrium, we find that $\langle m_{ex}^y \rangle$ in Fig. 6(a) and $\langle m_{ex}^x \rangle$ in Fig. 6(b) both have appreciable values close to the contacts and extend into the system only over L_c before the quasiparticle wave functions decay and the supercurrent associated with the BEC flows in the system to conserve current. In particular, it should be noted that the value of $\langle m_{ex}^x \rangle$ is quite close to the value of the on-site Coulomb term, U. However, when we increase the interlayer voltage to 1500 mV in Fig. 7 we are now driving the system beyond the critical current and the directional pseudospin fields are very different. In Fig. 7(a) we plot $\langle m_{ex}^y \rangle$ instead of taking on a value which is greater than that of $\langle m_{ex}^x \rangle$, shown in Fig. 7(b), it is now zero over the entire system. Furthermore, $\langle m_{ex}^x \rangle$ is no longer on the same order as U instead it is very close to the value of Δ_{sas} and is nonzero over the entire system. Therefore, the system is no longer driving a BEC with a transport gap about the Fermi energy but rather the two layers are acting as independent Fermi surfaces connected only by the weak single-particle interaction.

We solidify this assertion by examining the behavior of the order parameter above and below the critical current. In Fig. 8 we plot the order parameters for interlayer voltages of $V_{interlayer}=1$ mV (solid black) and $V_{interlayer}=1500$ mV (dotted red) down the center line of the system with $V_{tg}=-V_{bg}=400$ mV. The order parameter for the applied bias of 1 mV is nonzero across the length of the system and has a slope which is proportional to superfluid velocity. The slope of the order parameter is not constant near the center of the system

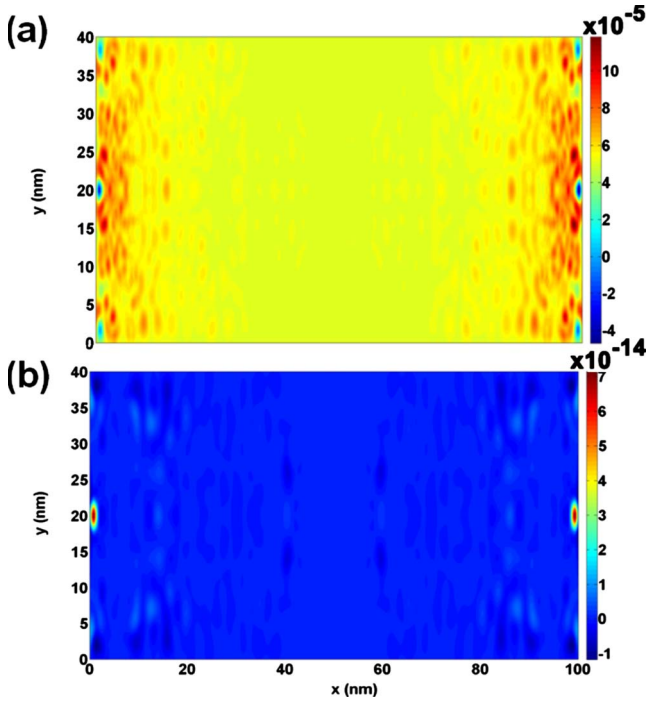

FIG. 7. (Color online) Surface plots of the directional pseudospin fields (a) $\langle m_{ex}^{x} \rangle$ and (b) $\langle m_{ex}^{y} \rangle$ computed from the self-consistent density matrix for a 40-nm-wide graphene bilayer with $V_{tg}=-V_{bg}=400$ mV for interlayer voltage of $V_{interlayer}=1500$ mV. We are beyond the critical current and the pseudospin fields are reduced in value and penetrate throughout the system. The scales for the figures are in electron volt.

due to the fact that we have included a single-particle tunneling amplitude, Δ_{sas}. The single-particle tunneling term tries to force a constant phase across the system and this competes with the superfluid flow which wants a constant gradient in the phase. This is contrasted by the order parameter corresponding to the interlayer voltage of 1500 mV where we find a that the order parameter is zero across the entire system. This clearly demonstrates the loss of the BEC

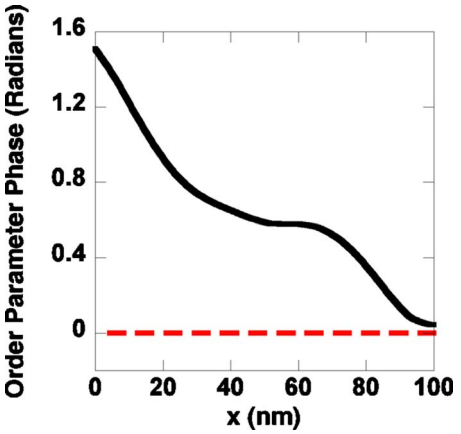

FIG. 8. (Color online) Plot of the value of the order parameter through the centerline of the system with $V_{tg}=-V_{bg}=400$ mV for interlayer voltages of $V_{interlayer}=1$ mV (solid black) and $V_{interlayer}=1500$ mV (dotted red).

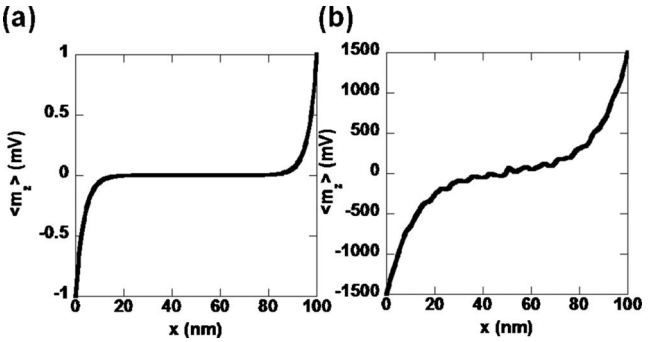

FIG. 9. Plot of the pseudospin torque term, $\langle m_{ex}^{z} \rangle$, through the centerline of the system with $V_{tg}=-V_{bg}=400$ mV for interlayer voltages of (a) $V_{interlayer}=1$ mV and (b) $V_{interlayer}=1500$ mV.

and the associated gap as well as the appearance of two incoherent, noninteracting Fermi liquids in Fig. 7.

We conclude this section by examining the interaction term which represents the pseudospin torque effect, the $\langle m_{ex}^{z} \rangle$ term. In Fig. 9(a), we plot the pseudospin torque term while the system is still below the critical current and so the system is in an ordered pseudospin state. We see very clearly that as the quasiparticle current enters the system the interactions resulting from the pseudospin torque effect, described in Eq. (10), work to shift the pseudospin "up," $|\uparrow\rangle$, to pseudospin "down," $|\downarrow\rangle$ along the pseudospin Bloch sphere at the left-hand side of the sample and from pseudospin up, $|\downarrow\rangle$, to pseudospin down, $|\uparrow\rangle$ at the right-hand side of the system. The pseudospin torque term only acts on the quasiparticles over a distance of L_c on the left- and right-hand sides of the system after which $\langle m_{ex}^{z} \rangle$ decays to zero at which point the quasiparticle current is converted into the supercurrent which flows in the bulk. This picture is to be contrasted with Fig. 9(b), where the system is now biased past the critical current and we are no longer in an ordered pseudospin state. Now we notice that the pseudospin torque term, $\langle m_{ex}^{z} \rangle$, is nonzero over the entire length of the system giving indicating a precession about the pseudospin Bloch sphere which is occurring everywhere in the system due to single-particle tunneling effects rather than the collective effects observed in Fig. 9(a). Further, we also observe the effects of a lack of self-consistency between the mean-field equations which has manifested itself in the oscillations of $\langle m_{ex}^{z} \rangle$ toward the center of the system.

B. Finite-temperature results

While the low-temperature results are consistent with the simple theory outlined earlier, problems arise when we raise the system temperature to room temperature. We begin again by examining the order parameter to determine whether or not we have a condensate present in our system at a given gate voltage bias on the top and bottom contacts. As in the previous section, we set the gate voltages to be $V_{tg}=-V_{bg}=400$ mV and the temperature to 300 K. In Fig. 10, we plot the order parameter across the centerline of the system, as in the previous section. As in Fig. 2 for the low-temperature case, we find that the order parameter assumes a nonzero value across the length of the system. We find that in the

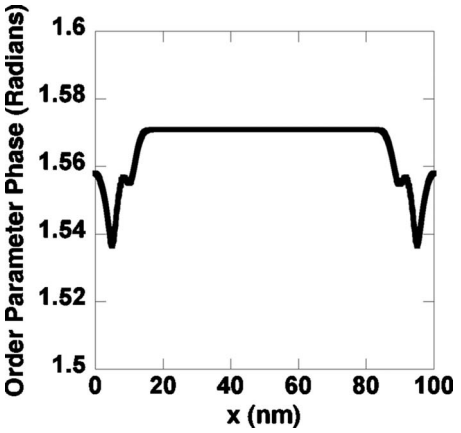

FIG. 10. Plot of the value of the order parameter for 40-nm-wide layers through the centerline of the system with $V_{tg}=-V_{bg}=400$ mV at room temperature while the system is in equilibrium.

room-temperature case, the deviations away from $\frac{\pi}{2}$ are smaller than in the low-temperature case and are typically around 5% with the largest variations occurring near the middle of the contact regions. The reduction in the variations in the order parameter is due to the thermal smearing of the states. In the room-temperature case the reflections of the gapped region are smoothed out due to thermal smearing which results in an order parameter with less variation.

The smoother order parameter brings about additional changes to the system. These changes can be seen in the directional pseudospin fields. In Fig. 11, we plot (a) $\langle m_{ex}^{x} \rangle$ and (b) $\langle m_{ex}^{y} \rangle$ corresponding to the 40-nm-wide bilayer graphene system in equilibrium. We notice that while the magnitude of the plots are very similar to their low-temperature counterparts, the penetration of the quasiparticles into the gapped region now reaches approximately 25 nm where previously is was tightly held to the coherence length, L_c. While the reduction in the spatial variations in the quasiparticle wave functions are attributed to the thermal smearing, the increased penetration observed here is due to the non-negligible contributions to the density matrix arising from the occupation of subbands well above the gapped region in the energy spectrum. These wave functions couple between the top and bottom layers without seeing the excitation gap and, therefore, can have nonzero value within the region that is gapped for low-energy excitations. While the most dramatic results are seen near the contacts, where the greatest contribution from the quasiparticle current flow is seen, there are nonzero contributions from these thermally excited contributions which exist throughout the system.

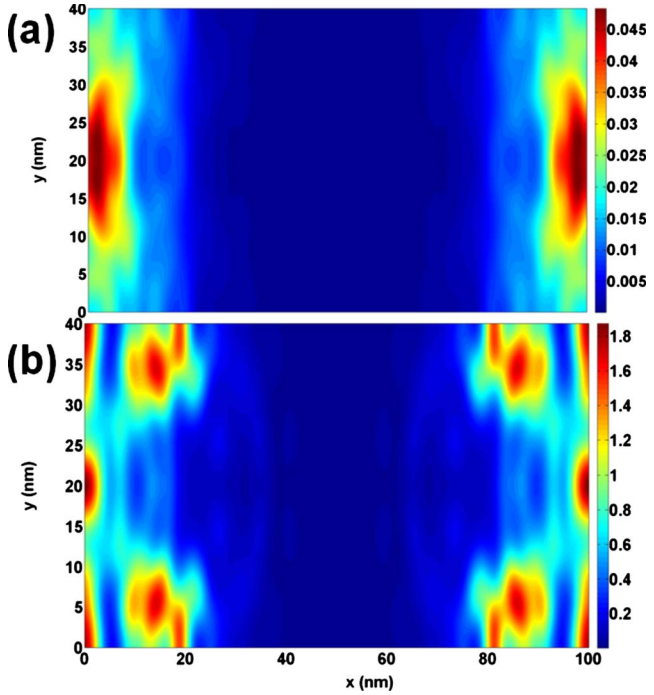

FIG. 11. (Color online) Surface plots of the directional pseudospin fields (a) $\langle m_{ex}^{x} \rangle$ and (b) $\langle m_{ex}^{y} \rangle$ computed from the self-consistent density matrix for a 40-nm-wide graphene bilayer with $V_{tg}=-V_{bg}=400$ mV in equilibrium at $T=300$ K. The scales for the figures are in electron volt.

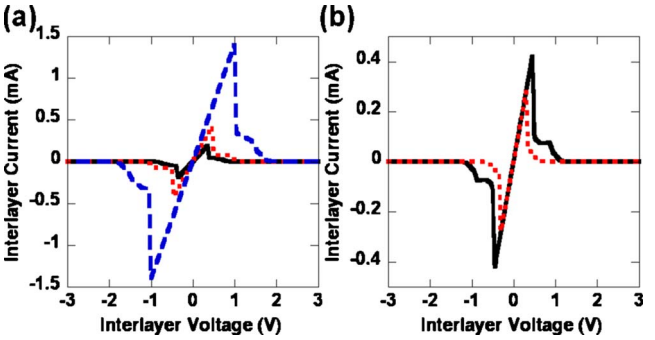

FIG. 12. (Color online) (a) Plot of the interlayer current versus the applied interlayer voltage for gate voltages of $V_{tg}=-V_{bg}=200$ mV (solid black), 400 mV (dotted red), and 600 mV (dashed blue) for a system temperature of 300 K. (b) Plot of the interlayer current for gate voltages of $V_{tg}=-V_{bg}=400$ mV for system temperatures of 0 K (dotted red) and 300 K (solid black). The inset shows the differential conductance as a function of the applied interlayer voltage for $V_{tg}=-V_{bg}=400$ mV for system temperatures of 0 K (dotted red) and 300 K (solid black). Note that the 300 K case allows for higher critical currents as is evidenced by the extended flat region of the differential conductance as compared to that of the low-temperature case.

With clear evidence of a BEC, we once again examine the interlayer transport properties at finite bias. In Fig. 12, we plot the interlayer current from the top left contact to the bottom right contact as a function of the applied interlayer voltage. In Fig. 12(a), we plot the interlayer current versus the applied interlayer voltage for gate voltage values of $V_{tg}=-V_{bg}=200$, 400, and 400 mV. We see that the general form of the transfer characteristics maintain the same form as the low-temperature plots but the magnitude of the interlayer current is significantly larger. This is made much more evident in Fig. 12(b), where we plot the interlayer current against the applied interlayer voltage for $V_{tg}=-V_{bg}=400$ mV for both the low-temperature and the high-temperature cases. It is clear that at high temperature the system is allowed to reach much higher currents than at low temperature. As thermally excited subband contributions ex-

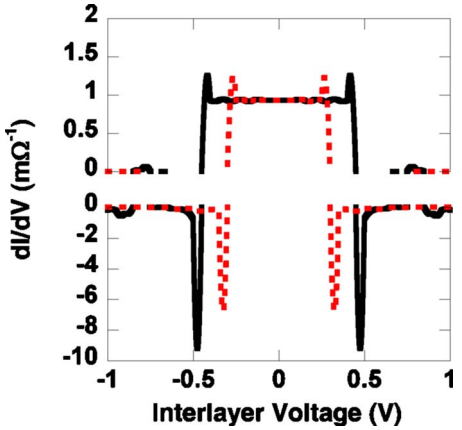

FIG. 13. (Color online) Plot of the differential tunneling conductance as a function of the applied interlayer voltage for $V_{tg}=-V_{bg}=400$ mV for system temperatures of 0 K (dotted red) and 300 K (solid black). Note that the 300 K case allows for higher critical currents as is evidenced by the extended flat region of the differential conductance as compared to that of the low-temperature case.

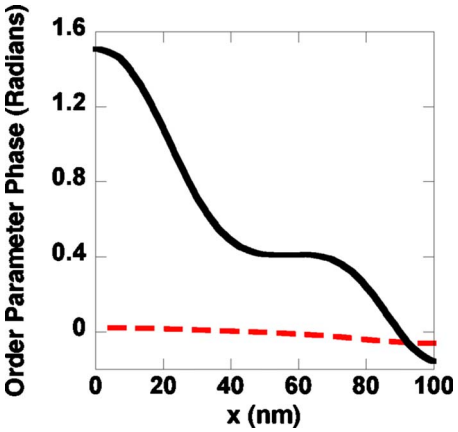

FIG. 14. (Color online) Plot of the value of the order parameter for 40-nm-wide layers at a width of 20 nm down the length of the system with $V_{tg}=-V_{bg}=400$ mV at an interlayer bias of $V_{interlayer}=350$ mV for a system temperature of $T=300$ K (solid black) and $T=0$ K (dotted red).

ist throughout the system this leads to some locally enhanced directional pseudospin fields inside the gapped region which results in an increased contribution to the interlayer transport from the single-particle incoherent tunneling as compared to the low-temperature case, however, the contribution from these higher subbands is dwarfed in magnitude by the coherent contribution to the current. This phenomenon could explain the prolonged difference in the decay of the interlayer current past the critical current.

Nevertheless, it is not possible to ascertain the location of the critical current from plots of the interlayer current versus the applied interlayer voltage. Instead, we look to Fig. 13 where we plot the differential conductance versus the applied bias. This gives a very clear picture of the extension of the region of constant current increase with increasing voltage to approximately $|V_{crit}|=35$ mV, $|V_{crit}|=0.45$ mV, and $|V_{crit}|=1$ V resulting in critical currents of $|I_{crit}|=109.4\pm7.4$, 419.7 ± 12.3 μA, and 1.40 ± 0.1 mA.

To explain the discrepancy between the predicted values and the values obtained, we examine the behavior of the system parameters as we have done in the previous section. Nevertheless, a simple examination of the room-temperature behavior below and above the calculated critical currents will not give any insight into the explanation for what allows a bilayer graphene system to reach higher critical currents at room temperature as opposed to low temperature. We facilitate the analysis by inspecting these quantities at the last interlayer voltage where, at room temperature, we achieve self-consistent solutions for the density matrix at $V_{interlayer}=350$ mV. We begin by examining the order parameter in Fig. 14. We find that the order parameter calculated for the room-temperature system exhibits the linear slope near the edges corresponding to the nonzero condensate velocity and the much smaller slope in the center of the system resulting from the inclusion of the single-particle tunneling. This order parameter is very similar in shape to the one presented in Fig. 8 which was calculated with $T=0$ K but at $V_{interlayer}=1$ mV. Where as the order parameter corresponding to the low-temperature case has almost no gradient to it which tells us that most of the current carried in this system is being carried by incoherent single-particle tunneling rather than the spontaneously coherent situation when we are driving the BEC.

The behavior of the order parameter shows us that in the room-temperature case we can maintain the condensate flow to higher interlayer voltages but it gives us no insight as to how this is able to occur. Examination of the in-plane directional pseudospin fields $\langle m_{ex}^x\rangle$ and $\langle m_{ex}^y\rangle$ only reveal the same type of behavior seen in the low-temperature data presented in Fig. 6. Namely, for the high-temperature case where the current transported in between the two layers coherently, due to the presence of a BEC, we see a large $\langle m_{ex}^y\rangle$ and $\langle m_{ex}^x\rangle$. Both $\langle m_{ex}^y\rangle$ and $\langle m_{ex}^x\rangle$ are large in value with $\langle m_{ex}^y\rangle$ obtaining a self-consistent value close to that of U and with $\langle m_{ex}^y\rangle$ being approximately one order of magnitude greater than that of $\langle m_{ex}^x\rangle$. When we examine the low-temperature data, we find that $\langle m_{ex}^y\rangle$ is very close to zero and $\langle m_{ex}^x\rangle$ takes on the value of Δ_{sas} over the entire system corresponding to a situation where the interlayer transport is now incoherent and the two layers function as if they are noninteracting. Yet, this analysis still offers us no insight into the reason for the discrepancy between the finite- and zero-temperature systems.

Instead, we seek the answer not through the examination of the properties of the density matrix when one of the systems is past the critical current and the other is not but by looking to $\langle m_{ex}^z\rangle$. In Fig. 15(a), we plot the interlayer current for temperatures of 0 K (dashed red), 150 K (dotted blue), and 300 K (solid black) with $V_{tg}=-V_{bg}=400$ mV. We see very clearly that as we increase the system temperature the value of the critical current begins to increase from the theoretically predicted value. We choose the interlayer voltage of $V_{interlayer}=350$ mV as this bias point is the last point in which the system obtains a self-consistent solution to the coupled set of mean-field equations for all three temperatures. In Fig. 15(b), we plot $\langle m_{ex}^z\rangle$. When we compare the $T=0$ K and the $T=300$ K curves, the reason for the discrepancy becomes very clear. When the system is calculated at

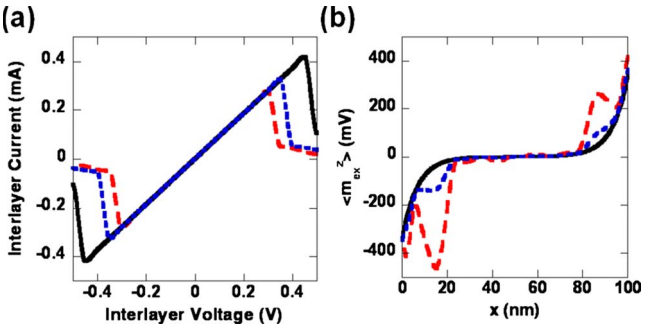

FIG. 15. (Color online) (a) Plot of the value of the interlayer current for temperatures of 0 K (dashed red), 150 K (dotted blue), and 300 K (solid black) with $V_{tg}=-V_{bg}=400$ mV showing the extension of the bias region for which the system is spontaneously coherent as the temperature is increased. (b) Plot of the pseudospin torque term, $\langle m_{ex}^z \rangle$, plotted down the centerline of the bilayer system for temperatures of 0 K (dashed red), 150 K (dotted blue), and 300 K (solid black) with $V_{tg}=-V_{bg}=400$ mV showing the smoothing of variations in the precession of the pseudospins about the Bloch sphere as the temperature is increased.

low temperature, there is a great deal of quantum interference from the reflections of the excitonic gap which interfere with other injected modes. These interferences result in oscillations in the quasiparticle density which enters into the Poisson equation to determine the electrostatic contribution to the potential. This results in a large oscillations in $\langle m_{ex}^z \rangle$ especially near the contacts. Therefore, a contribution to the system with large local variations enters into the Hamiltonian and serves to separate the two layers in energy causing the system to reach critical current more quickly as the interlayer voltage is increased. However, when the system temperature is raised to $T=300$ K, the thermal smearing produces a very uniform quasiparticle density in each of the layers. This distribution results in $\langle m_{ex}^z \rangle$ without the potential fluctuations, which can be significant at lower temperatures.

IV. SUMMARY AND CONCLUSIONS

In conclusion, we have presented self-consistent quantum transport calculations of exciton transport in bilayer graphene at both zero and finite temperature. We have shown that the zero-temperature physics may be compactly explained by simple predictions made based on pseudospin torque model are able to predict the critical currents in bilayer graphene at $T=0$ K. Past the critical current not only did the interlayer conductivity drop significantly, as seen in both the directional pseudospin fields and the I-V characteristics, but we also lose the ability to obtain self-consistent solutions between the mean-field transport equations and the excitonic gap. When we examine the interlayer current, we find that above and below the critical current the majority of the interlayer current flows near the contacts but above critical current. However, above critical current, there is some current flow throughout the device whereas below critical current there is only current flow between the layers a distance of L_c from the contacts. We have also shown that when the system temperature is raised to finite temperatures important differences arise which are not captured in the analytical models. We find that the quasiparticle wave functions are capable of penetrating the forbidden gap farther due to the excitation of modes far away from the energy gap coupling between the two layers. Further, we find that the critical currents are much larger at finite temperature due to thermal smoothing of the $\hat{z}$-directed pseudospin field which leads to a reduction in the value of the pseudospin torque term.

ACKNOWLEDGMENTS

The author is grateful for and has benefited significantly from conversations with A. H. MacDonald, G. Baym, D. Goldhaber-Gordon, W. Dietsche, L. Tiemann, and S. Schmult. This work supported by ARO.

*matthewg@illinois.edu

[1] O. Gunawan, Y. P. Shkolnikov, E. P. De Poortere, E. Tutuc, and M. Shayegan, Phys. Rev. Lett. **93**, 246603 (2004).
[2] R. D. Wiersma, J. G. S. Lok, S. Kraus, W. Dietsche, K. von Klitzing, D. Schuh, M. Bichler, H. P. Tranitz, and W. Wegscheider, Phys. Rev. Lett. **93**, 266805 (2004).
[3] M. Kellogg, J. P. Eisenstein, L. N. Pfeiffer, and K. W. West, Phys. Rev. Lett. **93**, 036801 (2004).
[4] M. Kellogg, I. B. Spielman, J. P. Eisenstein, L. N. Pfeiffer, and K. W. West, Phys. Rev. Lett. **88**, 126804 (2002).
[5] R. D. Wiersma, J. G. S. Lok, S. Kraus, W. D. K. von Klitzing, D. Schuh, M. Bichler, H. P. Tranitz, and W. Wegscheider, Physica E **34**, 16 (2006).
[6] R. Pillarisetty, H. Noh, E. P. DePootere, D. C. Tsui, and M. Shayegan, Physica E **22**, 300 (2004).
[7] H. A. Fertig, Phys. Rev. B **40**, 1087 (1989).
[8] X. G. Wen and A. Zee, Phys. Rev. Lett. **69**, 1811 (1992).
[9] K. Moon, H. Mori, K. Yang, S. M. Girvin, A. H. MacDonald, L. Zheng, D. Yoshioka, and S. C. Zhang, Phys. Rev. B **51**, 5138 (1995).
[10] B. I. Halperin, P. A. Lee, and N. Read, Phys. Rev. B **47**, 7312 (1993).
[11] D. V. Fil and S. I. Shevchenko, Low Temp. Phys. **33**, 780 (2007).
[12] K. Park and S. Das Sarma, Phys. Rev. B **74**, 035338 (2006).
[13] O. L. Berman, R. Y. Kezerashvili, and Y. E. Lozovik, Nanotechnology **21**, 134019 (2010).
[14] R. Côté, D. B. Boisvert, J. Bourassa, M. Boissonneault, and H. A. Fertig, Phys. Rev. B **76**, 125320 (2007).
[15] A. Stern, S. M. Girvin, A. H. MacDonald, and N. Ma, Phys. Rev. Lett. **86**, 1829 (2001).
[16] L. Balents and L. Radzihovsky, Phys. Rev. Lett. **86**, 1825 (2001).
[17] G. Murthy and S. Sachdev, Phys. Rev. Lett. **101**, 226801 (2008).
[18] M. M. Fogler and F. Wilczek, Phys. Rev. Lett. **86**, 1833 (2001).
[19] S. He, S. Das Sarma, and X. C. Xie, Phys. Rev. B **47**, 4394

(1993).
[20] A. H. MacDonald, Physica B **298**, 129 (2001).
[21] T. Jungwirth and A. H. MacDonald, Phys. Rev. Lett. **87**, 216801 (2001).
[22] Z. G. Koinov, Phys. Rev. B **79**, 073409 (2009).
[23] O. L. Berman, Y. E. Lozovik, and G. Gumbs, Phys. Rev. B **77**, 155433 (2008).
[24] H. K. Min, R. Bistritzer, J. J. Su, and A. H. MacDonald, Phys. Rev. B **78**, 121401 (2008).
[25] C. H. Zhang and Y. N. Joglekar, Phys. Rev. B **77**, 233405 (2008).
[26] M. J. Gilbert and J. Shumway, J. Comput. Electron. **8**, 51 (2009).
[27] M. Y. Kharitonov and K. B. Efetov, Phys. Rev. B **78**, 241401(R) (2008).
[28] E. Rossi, O. G. Heinonen, and A. H. MacDonald, Phys. Rev. B **72**, 174412 (2005).
[29] A. Nunez and A. H. MacDonald, Solid State Commun. **139**, 31 (2006).
[30] P. Haney, R. Duine, A. Nunez, and A. MacDonald, J. Magn. Magn. Mater. **320**, 1300 (2008).
[31] L. Tiemann, W. Dietsche, M. Hauser, and K. von Klitzing, New J. Phys. **10**, 045018 (2008).
[32] L. Tiemann, Y. Yoon, W. Dietsche, K. von Klitzing, and W. Wegscheider, Phys. Rev. B **80**, 165120 (2009).
[33] J. J. Su and A. H. MacDonald, Nat. Phys. **4**, 799 (2008).
[34] T. Ando, Physica E **20**, 24 (2003).
[35] T. Ando, Physica E **40**, 213 (2007).
[36] M. Abolfath, L. Radzihovsky, and A. H. MacDonald, Phys. Rev. B **65**, 233306 (2002).
[37] W. H. Rippard, M. R. Pufall, and S. E. Russek, Phys. Rev. B **74**, 224409 (2006).
[38] S. H. Abedinpour, M. Polini, A. H. MacDonald, B. Tanatar, M. P. Tosi, and G. Vignale, Phys. Rev. Lett. **99**, 206802 (2007).
[39] A. Rycerz, J. Tworzydlo, and C. W. J. Beenakker, Nat. Phys. **3**, 172 (2007).
[40] T. Ando, Phys. Rev. B **44**, 8017 (1991).
[41] D. D. Johnson, Phys. Rev. B **38**, 12807 (1988).
[42] B. I. Halperin, Helv. Phys. Acta **56**, 75 (1983).
[43] J. P. Eisenstein and A. H. MacDonald, Nature (London) **432**, 691 (2004).
[44] Y. Yoon, L. Tiemann, S. Schmult, W. Dietsche, K. von Klitzing, and W. Wegscheider, Phys. Rev. Lett. **104**, 116802 (2010).